Letter | Editors' Suggestion

Observation of chiral domain walls in an octupole-ordered antiferromagnet

Moeta Tsukamoto,[1,*] Zhewen Xu,[2] Tomoya Higo,[1] Kouta Kondou,[3] Kento Sasaki,[1] Mihiro Asakura,[1] Shoya Sakamoto,[4] Pietro Gambardella,[5] Shinji Miwa,[4,6] YoshiChika Otani,[3,4,6] Satoru Nakatsuji,[1,4,6] Christian L. Degen,[2] and Kensuke Kobayashi[1,6,7,†]

[1]*Department of Physics, The University of Tokyo, Bunkyo, Tokyo 113-0033, Japan*
[2]*Department of Physics, ETH Zurich, Otto-Stern-Weg 1, 8093 Zurich, Switzerland*
[3]*RIKEN, Center for Emergent Matter Science (CEMS), Saitama 351-0198, Japan*
[4]*Institute for Solid State Physics, The University of Tokyo, Kashiwa, Chiba 277-8581, Japan*
[5]*Department of Materials, ETH Zurich, Honggerbergring 64, 8093 Zurich, Switzerland*
[6]*Trans-Scale Quantum Science Institute, The University of Tokyo, Bunkyo, Tokyo 113-0033, Japan*
[7]*Institute for Physics of Intelligence, The University of Tokyo, Bunkyo, Tokyo 113-0033, Japan*

(Received 24 October 2024; revised 10 April 2025; accepted 5 June 2025; published 17 July 2025)

Spin chirality in antiferromagnets offers new opportunities for spintronics. The kagome antiferromagnet Mn_3Sn is a paradigmatic material in which the antiferromagnetic order parameter can be detected and controlled by electrical means. However, direct investigation of the magnetic texture of Mn_3Sn has been challenging because of the tiny moment hosted in its magnetic octupole, hindering further clarification of this unique material. Here, we address this issue by observing the stray magnetic field from Mn_3Sn using a diamond-based quantum scanning microscope. The spatially resolved intrinsic domains and domain walls in a high-quality single-crystalline Mn_3Sn film quantitatively reveal the polarization angle of the magnetic octupole in the kagome plane, the domain's local magnetization, the domain wall's width and chirality, and the octupole order in domain walls. Our nanoscale investigation of Mn_3Sn, a powerful complement to macroscopic measurements, paves the road for developing chiral antiferromagnetism and its potential for spintronic applications.

DOI: 10.1103/njnm-nl6n

Antiferromagnets (AFs) are promising candidates for realizing high-speed and high-density spintronic devices thanks to their intrinsic terahertz spin dynamics and tiny stray magnetic fields [1,2]. In recent years, much work has been done on the noncollinear AF Mn_3Sn as an ideal platform for AF spintronics [3–12]. Mn_3Sn, characterized by a cluster magnetic octupole, has vanishingly small net magnetization yet shows a giant anomalous Hall effect comparable to ferromagnetic materials, reflecting the Berry curvature emerging from the pair of Weyl points in its topological band structure [13]. The same feature also leads to an appreciable anomalous Nernst effect [14,15]. The recently reported tunnel magnetoresistance effect [16] based on the octupole order [8] further enhances the attraction of this unique material for device applications.

In light of the history of conventional ferromagnet-based spintronics [17,18], the importance of a quantitative understanding of the magnetic domains in AFs cannot be overemphasized. The dynamics of an antiferromagnetic domain are expected to depend on domain wall (DW) chirality (Fig. 1), influencing the manipulation in spintronic devices [18–20]. Mn_3Sn film is also promising in this direction [21]. Based on the fundamental research of magnetic octupoles [22–26], electrical manipulation of the magnetization has been demonstrated using spin-orbit and spin-transfer torque [7,11,21,27–29], and the piezomagnetic effect [30]. Obtaining more detailed physical insight into the magnetic domains would accelerate device applications [17,21,31,32]. Particularly for AFs, focusing on the DWs is an effective strategy since they locally break the magnetic symmetry, resulting in an observable stray field. However, the observation of AF DWs and their chirality are experimentally challenging. For Mn_3Sn, magnetic force microscopy only provides qualitative information [33], while the optical resolution of the magneto-optical Kerr effect (MOKE) measurement is not sufficiently detailed [32,34,35]. Recent magnetic field measurements by diamond-based quantum scanning microscope (QSM) are promising, as they provide new insights into the DWs of model AF such as Cr_2O_3 [19,36,37]; for Mn_3Sn, despite pioneering observations of polycrystalline samples [38], a quantitative investigation has thus far been lacking.

Here, we report detailed observations of the magnetic domains and chiral DWs in a high-quality single-crystalline Mn_3Sn film using QSM. A stray magnetic field from the film directly probes the magnetic octupole ordering in the domains. The simultaneous detection of the weak magnetization, its axis, and its behavior in the DWs further reveals the nature of the magnetic octupole. Significantly, the observed DWs, which we determine to be of left Néel type (top panel of Fig. 1) with a width as narrow as ∼40 nm, clearly show how the octupole moment performs a chiral rotation in the kagome plane of Mn_3Sn. Our findings will further advance the understanding and control of magnetic octupoles in chiral AFs.

*Contact author: moeta.tsukamoto@edu.k.u-tokyo.ac.jp
†Contact author: kensuke@phys.s.u-tokyo.ac.jp

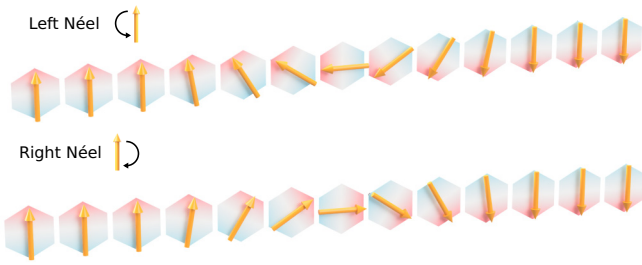

FIG. 1. Octupole-ordered chiral domain wall. Schematic illustration of left Néel wall (top) and right Néel wall (bottom). Hexagons indicate the cluster magnetic octupoles, and orange arrows correspond to the octupole moments [also see Fig. 2(b)]. The film structure, shown in Fig. 2(a), breaks the vertical direction symmetry, defining the chirality.

We use a thin Mn_3Sn film with a thickness $t = 20$ nm grown on a 7-nm-thick W buffer layer on an MgO substrate, capped by a 5-nm-thick MgO layer, as shown in Fig. 2(a). The films are grown by molecular beam epitaxy. In Mn_3Sn, the Mn atom forms a kagome lattice and takes an antichiral triangular spin configuration. As a consequence, the net magnetization is vanishingly small at room temperature [24,25]. Nevertheless, a slight canting of the spins polarizes a magnetic octupole consisting of six Mn spins [Fig. 2(b)], which results in a detectable magnetic field because they acts as effective magnetic dipoles for QSM [3,8]. The ferroic order between them induces a macroscopic magnetization [8]. The x-ray diffraction data presented in Figs. 2(c) and 2(d) indicate well-aligned kagome planes. The MOKE result indicates that the coercive field of the film is ∼300 mT [Fig. 2(e)]. Microscopic observation of magnetic domains using MOKE suggests that the crystal grains of the film are several micrometers in size [7]. These results confirm the high crystallinity of the present film. While the easy axis in the pristine Mn_3Sn is $\langle 2\bar{1}\bar{1}0\rangle$, the insertion of the W buffer layer increases the perpendicular magnetic anisotropy so that the easy axis in our film is parallel to $[01\bar{1}0]$ [7].

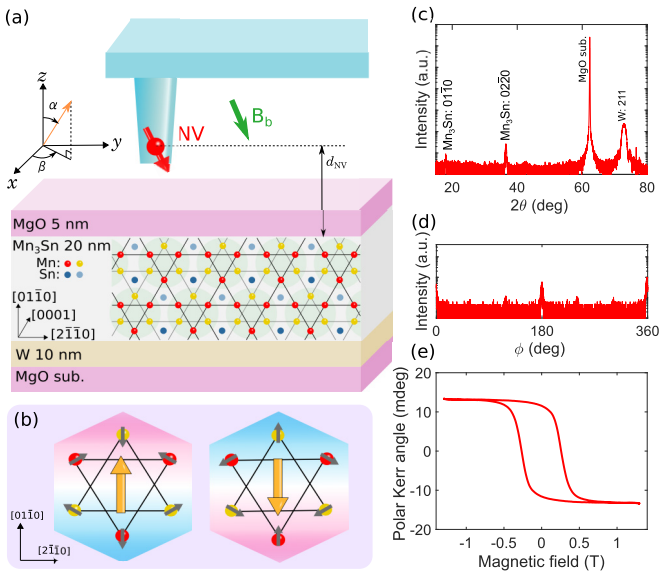

FIG. 2. Mn_3Sn thin film and quantum magnetometry. (a) Schematic of the sample and QSM tip. The AB stacking of the crystal lattice is shown inside the Mn_3Sn film, where the Mn atoms in each layer form the kagome lattice. For QSM, we use a single NV center embedded in the tip, shown by a thick red arrow. The bias field B_b, shown by a green arrow, is applied along the NV symmetry axis. The angles α and β, defined by the orange arrow, are used to analyze the magnetization direction (see text). (b) Schematic of the cluster magnetic octupole. Each octupole consists of six neighboring Mn spins, indicated by the green shading in (a). The gray and orange arrows indicate the dipole moment of Mn spin and the octupole moment, respectively. The octupole moment direction is upward and downward in the left and right panels, respectively, perpendicularly to the film surface $(01\bar{1}0)$. (c) and (d) XRD 2θ-scan and ϕ-scan data of the Mn_3Sn thin film, respectively. (e) Hysteresis behavior for the z-axis magnetic field measured by MOKE using 660 nm light at room temperature.

Figure 2(a) also shows a schematic of our QSM (QZabre LLC). The magnetic probe consists of a single nitrogen-vacancy (NV) center embedded in a diamond pillar attached to the tuning fork of the atomic force microscope. A magnetic field, when present, shifts the discrete energy levels of the NV center by the Zeeman effect. The shift can be determined by optically detected magnetic resonance using a confocal microscope. The technique enables us to obtain quantitative and three-dimensional vector information on the magnetic field felt by the NV center [19]. The NV center scans the xy plane at a height of d_{NV} [Fig. 2(a)], defined by the distance between the NV center and the top surface of Mn_3Sn film, yielding the spatial distribution of the magnetic stray field of the sample. In our work, d_{NV} is approximately 60 nm, determining the spatial resolution of the imaging (see Sec. I in Ref. [39] for details). For measurement's sake, the external bias field B_b is applied parallel to the NV axis [Fig. 2(a)]. All measurements are performed at room temperature.

Figure 3(a) shows an image plot of the z-axis projection of the magnetic field B_z, i.e., the stray field perpendicular to the film surface, where the contribution of B_b has been subtracted. Most of the image is covered by red and blue regions, corresponding to areas where the field is positive and negative, respectively. This implies magnetic domain formation due to the perpendicular magnetic anisotropy. The field changes steeply at the white lines (zero stray fields) between the red and blue regions, revealing the DWs. We also observe regions with tiny stray fields (white regions) on the right side of the image. These may be due to undeveloped magnetic domains or a different magnetization structure from the rest of the image. From now on, we will focus on the regions with strong magnetic contrast. The absolute value of the observed stray field from our 20-nm-thick film is only about 0.6 mT. For comparison, the previous QSM measurement [40] reported stray fields ∼1 mT for a ferromagnet CoFeB film as thin as 1 nm. Therefore the present film has a weak magnetization.

Notably, the magnetic domains tend to elongate along the [0001] direction, consistent with a previous MOKE observation [35]. Such a distinctive phenomenon most likely reflects the easy-plane anisotropy of Mn_3Sn. In particular, the domains in Fig. 3(a), enclosed by the dash-dot black line, are large and rectangular. A detailed investigation of them is expected to elucidate the local magnetization texture

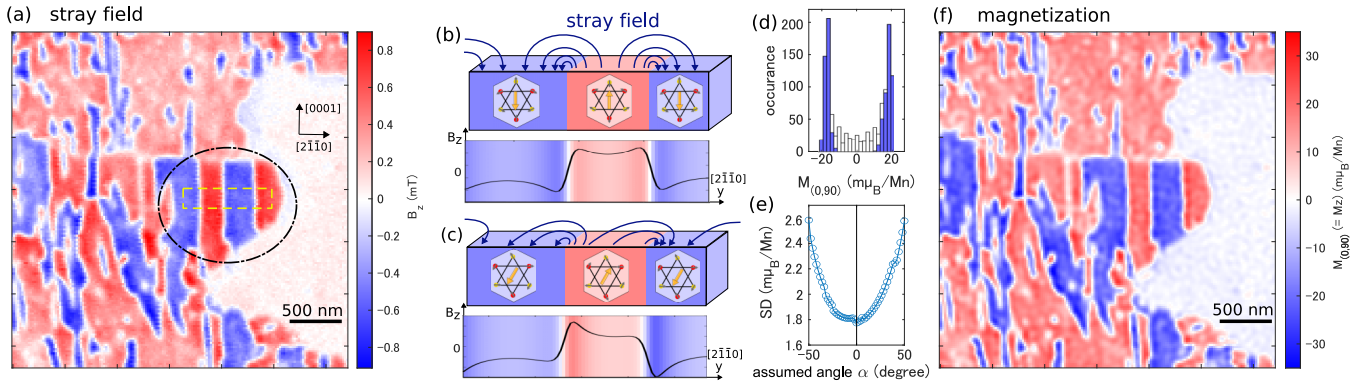

FIG. 3. Observed stray field and magnetization. (a) Image plot of the z-axis component of the magnetic stray field B_z. (b) and (c) Schematics of stray field from a perpendicular magnetization $\parallel [01\bar{1}0]$ and a 30° tilted magnetization $\parallel [\bar{1}\bar{1}20]$, respectively. The lower panels schematically show the corresponding B_z. The case (b) rather than (c) is realized in the present film. (d) Histogram analysis for the reconstructed magnetization in the area surrounded by the dashed yellow line in (a). Blue bars correspond to pixels well inside domains, while white bars are from pixels near the DW's. (e) Standard deviation of $|M_{(\alpha,90)}|$ of the blue peaks in (d) as a function of the assumed angle α. (f) Magnetization image reconstructed into the perpendicular orientation.

originating from the magnetic octupole. In this area, the stray field is almost constant inside the domains, implying that the magnetization is perpendicular to the surface [7]; Figure 3(b) schematically shows the stray field for the case with perpendicular magnetic anisotropy, agreeing with the previous observation [7]. On the other hand, if the magnetization were tilted [Fig. 3(c)], we should observe a field slanting in the domains, which is not the case in Fig. 3(a).

In the case of perpendicular magnetization, a well-known method exists for reconstructing stray fields to magnetization based on the Fourier transform [41,42]. However, for Mn_3Sn, a more careful analysis without such an assumption is required, as the theory predicts various magnetization directions different from a perpendicular orientation [8,43]. This analysis will confirm that the magnetization in Fig. 3(a) is predominantly out-of-plane.

First, we expand the existing method [41,42] to include tilted magnetization cases. We define $M_{(\alpha,\beta)}(x, y)$ as the magnetization value in the film at (x, y) and assume that it is uniaxial with the direction defined by the two angles, α and β, shown in Fig. 2(a). Scanning the NV center in the xy plane with $z = d_{\mathrm{NV}}$ fixed [Fig. 2(a)] enables us to obtain the magnetic field amplitude $B_{\mathrm{NV}}(x, y)$ at (x, y, d_{NV}). For a sufficiently thin magnetic film, the relation between the magnetization $\mathcal{M}_{(\alpha,\beta)}(k_x, k_y)$ and the magnetic field $\mathcal{B}_{\mathrm{NV}}(k_x, k_y)$ in the corresponding two-dimensional Fourier space is given by

$$\mathcal{M}_{(\alpha,\beta)} = \frac{1}{\tilde{g}(k, d_{\mathrm{NV}}, t)} \times \frac{k\mathcal{B}_{\mathrm{NV}}}{ik_x e_x + ik_y e_y - k e_z} \times \frac{1}{ik_x \sin\alpha\cos\beta + ik_y \sin\alpha \sin\beta - k\cos\alpha}, \quad (1)$$

where $\boldsymbol{e} = (e_x, e_y, e_z)$ is the unit vector to define the NV axis [the thick red arrow in Fig. 2(a)], (k_x, k_y) is a wave vector with $k = \sqrt{k_x^2 + k_y^2}$, and $\tilde{g}$ is a Green's function in Fourier space. The measured B_{NV} is converted to $\mathcal{B}_{\mathrm{NV}}$, then to $\mathcal{M}_{(\alpha,\beta)}$ using Eq. (1), and finally to $M_{(\alpha,\beta)}$ (see Secs. II and III in Ref. [39] for detail).

Next, we perform a histogram analysis of the statistical distribution of the obtained magnetization [44,45] to search for the most likely magnetization direction. Figure 3(d) shows the histogram obtained for the magnetization surrounded by the dashed yellow line in Fig. 3(a). Most data are clustered at either the positive or negative extremum, forming two sharp peaks with the same absolute value (blue bars). Meanwhile, values in-between reflect areas of low perpendicular magnetization near DWs (white). These observations imply that the domains in this area have antiparallel octupole moments of the same strength. Sharper peaks correspond to better binarization and, thus, a more likely case. Figure 3(e) plots the standard deviation of $|M_{(\alpha,90)}|$ obtained by varying α from $-50°$ to $50°$ with $\beta = 90°$ fixed for the same area. The fact that it is minimal at $\alpha = 0°$ indicates that a perpendicular magnetization is the most likely. We have repeated the same analysis assuming various possible combinations of α and β and have confirmed that $\alpha = 0°$ and $\beta = 90°$ give the smallest deviation. The resulting magnetization configuration is shown in Fig. 3(f). Our observations independently confirm [7] that inserting a W layer favors perpendicular magnetic anisotropy.

The magnetization obtained by averaging $|M_{(0,90)}|$ excluding DWs regions [Fig. 3(e)] is $17 \pm 2\,\mathrm{m}\mu_{\mathrm{B}}$/Mn. This value is two orders of magnitude smaller than the typical magnetization value of 1–3 μ_{B}/Mn in a Mn-based ferromagnet. Our value is about three times larger than the ~6 $\mathrm{m}\mu_{\mathrm{B}}$/Mn reported for a Mn_3Sn film by a standard magnetization measurement [7]. The difference is reasonable, as our QSM is performed on well-developed magnetic domains and not averaged over the entire film. Rather, our measurements demonstrate that the intrinsic nature of the material can be revealed by measuring high-quality portions with a precise local probe.

Systematic investigation of the response of Mn_3Sn to magnetic fields elucidates the nature of magnetic domains and DWs. Figures 4(a)–4(c) show the z projection of the stray field B_z when the bias magnetic field is sequentially varied from 9.5 to 26.5 to 10.2 mT, respectively. 100 mT is applied once between Figs. 4(b) and 4(c). The bias field is subtracted

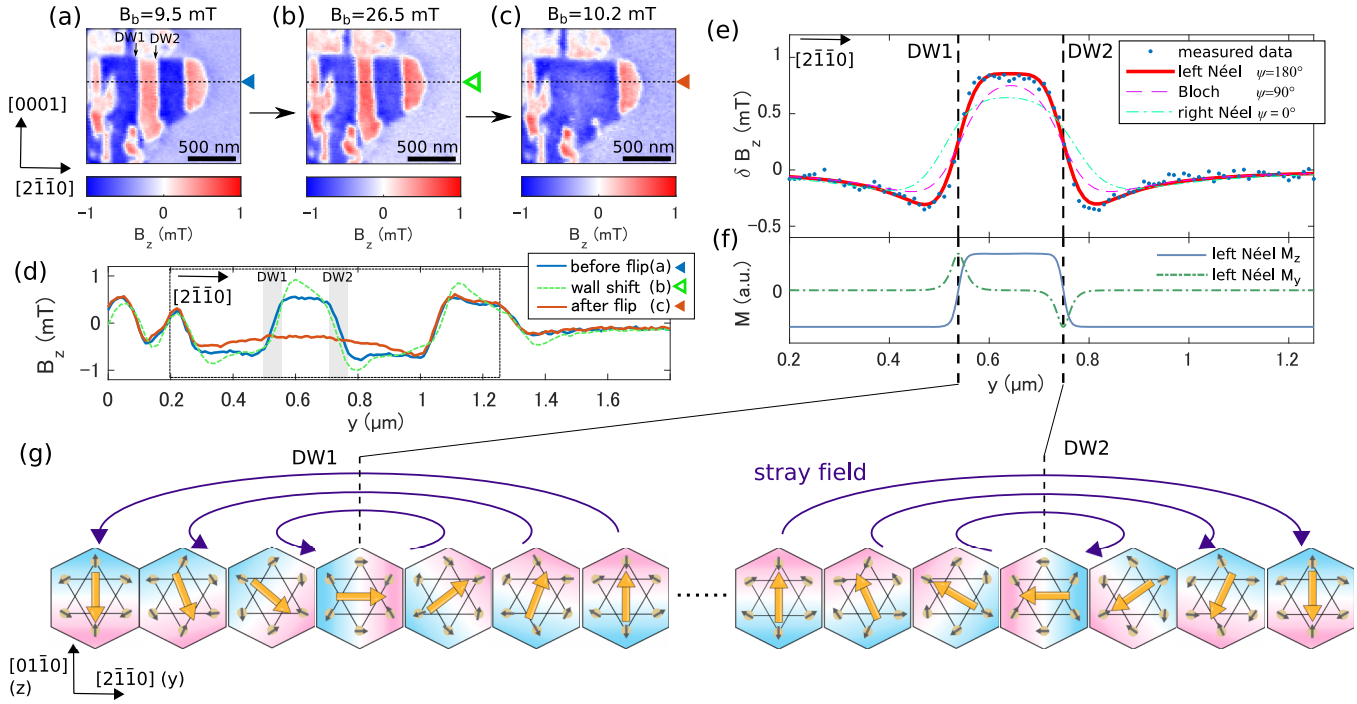

FIG. 4. Observation of chiral domain wall. [(a)–(c)] z projection of the stray field when the bias magnetic field is sequentially varied from 9.5 to 26.5 to 10.2 mT, respectively. 100 mT is applied once between (b) and (c). (d) Blue, green, and orange lines are cross-sections of the dashed black lines in (a), (b), and (c), respectively. DW1 and DW2 are indicated in a gray shade. (e) Shape of DW1 and DW2 extracted as the magnetic field difference between (a) and (c) is shown as blue dots. The fitted lines of left Néel ($\psi_i = 180°$), Bloch ($\psi_i = 90°$), and right Néel ($\psi_i = 0°$) walls are drawn by red, magenta, and cyan lines, respectively. (f) y and z projections of the magnetization of the left Néel fitting. Vertical black dashed lines indicate the positions of DW1 and DW2. (g) Schematics of magnetization and stray field lines near DW1 (left) and DW2 (right). The schematic of DW2 is equivalent to the top panel of Fig. 1.

in these images. The line scans at the black dashed lines in Figs. 4(a)–4(c) are shown in Fig. 4(d). As the bias field increases from Fig. 4(a) to Fig. 4(b), the blue (red) domains with the magnetization oriented parallel (antiparallel) to the field expand (shrink). The corresponding two DWs, DW1, and DW2, shift tens of nm along opposite [2$\bar{1}\bar{1}$0] directions, shown in Fig. 4(d). The fact that the DWs already move at $B_b = 26.5$ mT, a field much smaller than the coercivity of 300 mT [Fig. 2(e)], indicates that the DW dynamics are mainly governed by exchange interaction and magnetic anisotropy rather than by pinning potentials due to grain boundaries.

The red domain at the center vanishes in Fig. 4(c) after 100 mT is applied. The magnetization of this domain, initially surrounded by DW1 and DW2, flips in the same direction as the neighboring domains. The flipping field of the domain is at only one-third of the coercive field [measured by MOKE, Fig. 2(e)], again pointing toward on the intrinsic nature of the observed domains. The obtained field profile shown in Fig. 4(d) clarifies that the magnetic field far from this region is almost unchanged between Figs. 4(a) and 4(c), confirming the high reproducibility and the noninvasiveness of the QSM measurement. Thus we take the difference between the two for further analysis, as shown in Fig. 4(e) with blue dots. The resultant field δB_z originates purely from DW1 and DW2, corresponding to the octupole moment direction in the DWs. We notice that each wall width is significantly smaller than 200 nm, clearly much smaller than the reported wall width of ~630 nm [7,21].

We analyze the shape of the two DWs by fitting them using the conventional DW model given by [19,46,47]

$$M_x = -\frac{M_s \sin\psi}{\cosh\left(\frac{y-y_1}{\Delta_1}\right)} + \frac{M_s \sin\psi}{\cosh\left(\frac{y-y_2}{\Delta_2}\right)}, \tag{2}$$

$$M_y = -\frac{M_s \cos\psi}{\cosh\left(\frac{y-y_1}{\Delta_1}\right)} + \frac{M_s \cos\psi}{\cosh\left(\frac{y-y_2}{\Delta_2}\right)}, \tag{3}$$

$$M_z = M_s \tanh\left(\frac{y-y_1}{\Delta_1}\right) - M_s \tanh\left(\frac{y-y_2}{\Delta_2}\right) - M_s. \tag{4}$$

The fitting parameters are the positions y_i and widths $\pi\Delta_i$ of DWi ($i = 1, 2$), with the saturation magnetization M_s being common for DW1 and DW2. While the magnetization away from the DWs is parallel to the z direction, it has a finite xy-plane component characterized by the angle ψ inside DWs. $\psi = 0°$ corresponds to the positive direction of the y axis. The stray field from the DWs is determined by M_y and M_z due to the translational symmetry along the x axis ∥ [0001] direction. Fitting the DW model to the magnetic field data with $\psi = 180°$, as shown in red in Fig. 4(e), we obtain $M_s = 6.9 \pm 0.3$ kA/m $= 16.1 \pm 0.2\,\mathrm{m}\mu_\mathrm{B}$/Mn, $\Delta_1 = 13 \pm 3$ nm, and $\Delta_2 = 12 \pm 3$ nm. The obtained M_s is consistent with the $17 \pm 2\,\mathrm{m}\mu_\mathrm{B}$/Mn discussed above in Fig. 3. The

fittings with $\psi = 90^\circ$ and 0° shown in magenta and cyan lines in Fig. 4(e), respectively, are unsuccessful.

The observation of $\psi = 180^\circ$ tells us that the DWs are the left Néel type, rather than the right Néel type ($\psi = 0^\circ$) or the Bloch type ($\psi = 90^\circ$). In the Néel cases ($\psi = 0^\circ$ or 180°), $M_x = 0$ according to Eq. (2), and the octupole moments with constant magnitude rotate in the kagome plane around the x-axis. In the left Néel wall case, the moment at the DW center is horizontal and faces left when the upward magnetization region is placed on the left side (the top panel of Fig. 1). The spatial variations of the magnetization M_y and M_z are shown in Fig. 4(f). M_z changes its sign at the center of DWs, while M_y is finite only inside the DWs. There are several other theoretically possible DW structures [32,48]. We have performed fittings assuming that the magnetization can vary inside the DW and that the DWs split into several parts. The fittings confirmed that the left Néel type is the most likely to explain the observed magnetic field (see Sec. X in Ref. [39] for details). Figure 4(g) schematically depicts the structure of the DWs [31,33,49]. The octupole ordering in DWs suggests that the spins at each site in the octupole also have a ferroic order. While the magnetic field distribution depicted in Fig. 4(d) contains several DWs, rigorous analysis is possible only for DW1 and DW2 due to the interference of the fields from multiple DWs. To further support for the above interpretation, the observed distribution over 17 DWs can be quantitatively reproduced by assuming the left Néel-type DWs, eliminating the possibility of the right Néel-type (see Sec. XIII in Ref. [39] for details). Our data, therefore, suggest that the DWs along [0001] in this Mn_3Sn/W film are mainly of the left Néel-type type.

Theoretically, the DW width $\pi\Delta = \pi\sqrt{A/\kappa}$ along [0001] of Mn_3Sn is determined by minimizing the energy density [48],

$$\kappa = K + \tfrac{1}{2}\mu_0 M_s^2 \cos^2\psi + K_p \sin^2\psi, \tag{5}$$

where $A = 0.568$ meV/Å is the stiffness constant [43], $K = 1.4 \times 10^{-7}$ meV/Å^3 is the magnetic anisotropy [7], K_p is the in-plane anisotropy, ψ is the DW angle, and μ_0 is the vacuum permeability. The second term of Eq. (5) is the magnetostatic energy under zero magnetic field. The effect of bias magnetic field on Δ is neglected because Δ changes by at most 1 nm under the magnetic fields used in this study, which is smaller than the error bar of the fitting. We use $M_s = 6.9 \pm 0.3$ kA/m obtained above. The left Néel wall corresponds to $\psi = 180^\circ$. Thus, in Eq. (5), the third term is zero, while the second term is finite. This magnetostatic energy, in turn, is a hundred times larger than the magnetic anisotropy K, meaning that it determines the wall width. The DW width is predicted theoretically as $\Delta = 17 \pm 2$ nm, a value very close to the experimental result of Fig. 4(e). Considering that the calculation uses the known values except for M_s and ψ, the consistency validates the present result and analysis using the conventional DW model to Mn_3Sn. Further discussion, including the demagnetizing factor, suggests that the magnetostatic energy of a Néel DW is smaller than that of a Bloch wall [50]. This energy difference leads to a tendency for the domains to be separated by DWs running along the [0001] direction, resulting in the appearance of elongated domains as shown in Fig. 3(a) and the previous study [35] (see Sec. XII in Ref. [39] for detail).

We address the implication of the present experimental findings regarding AF spintronics applications of Mn_3Sn. The observation of the domains by QSM proves the existence of a perfectly perpendicular magnetization area, which maximizes the anomalous Hall effect and reduces the power consumption for readout. The observed magnetization of the well-developed domains is greater than previous values [16,21], promising accelerated writing and reading speed of devices. The coercive field, which is locally smaller than the area-averaged MOKE result, suggests a smaller threshold of intrinsic magnetization reversal than previous reports, enabling high-efficiency spin-orbit torque switching [7]. The identified left Néel wall chirality is crucial for developing DW devices, as the direction of current-induced DW motion depends on the chirality. The development of chirality may be due to the symmetry breaking in the vertical direction by inserting a W layer. Replacing W with other heavy metals, such as platinum, might invert the chirality and the DW motion direction. Considering that the DW width ultimately determines the device size, the narrow width of $\pi\Delta \sim 37$ nm obtained in our study redefines the integration limit and scalability of Mn_3Sn devices. These parameters can contribute to revealing the swapping trajectory of Weyl points at the DW, which was theoretically discussed recently [51,52]. Finally, the octupole ordering in DWs is the basis for clarifying the detailed mechanism of switching the octupole moment using spin transfer and spin-orbit torque.

To conclude, our QSM measurement experimentally established the weak magnetization, the direction of the octupole moment, and the chiral behavior of the moment inside the kagome plane of Mn_3Sn, all vividly illustrating the role of its cluster magnetic octupoles. While the weak magnetization of such thin films is challenging to measure, accurate values are obtained by the local method of QSM. The magnetic parameters provide quantitative input for the AF spintronics applications based on this material. The experimental proof of chiral DWs is a powerful complement to macroscopic measurements and further advances our understanding and control of chiral antiferromagnetism.

We thank S. Fukami, C. Broholm, Y. Araki, and A. Ozawa for useful discussions. The experiment was supported by QZabre LLC. This work was partially supported by Grants-in-Aid for Scientific Research (No. JP25H01248, No. JP24K21194, No. JP25H01248, No. JP24K21194, No. JP23K25800, No. JP22K03524, No. JP22KJ1059, and No. JP22J21412); Swiss National Science Foundation, Grants No. 200020_200465 and No. 200020_212051/1; Japan Science and Technology Agency, JST-CREST (JPMJCR23I2), JST-MIRAI Program (JPMJMI20A1), JST-ASPIRE (JPMJAP2317), Japan; Daikin Industries, Ltd.; Kondo Memorial Foundation; the Mitsubishi Foundation (Grant No. 202310021); the Cooperative Research Project of RIEC, Tohoku University. M.T. acknowledges financial support from World-leading Innovative Graduate Study Program

for Forefront Physics and Mathematics Program to Drive Transformation, The University of Tokyo. Z.X. acknowledges funding from the EU's Horizon 2020 programme (MSCA Grant No. 955671).

K.S., P.G., Y.O., S.N., C.L.D., and K. Kobayashi supervised the research; T.H., M.A., S.S., S.M., and S.N. grew the Mn_3Sn film; K. Kondou and Y.O. evaluated the film; M.T. and Z.X. performed QSM experiments; M.T., Z.X., and C.L.D. analyzed the data; M.T. and K. Kobayashi wrote the manuscript. All authors discussed the results and commented on the manuscript.

Data availability. The data used and analyzed during the current study available from corresponding authors on reasonable request.

[1] T. Jungwirth, X. Marti, P. Wadley, and J. Wunderlich, Antiferromagnetic spintronics, Nat. Nanotechnol. **11**, 231 (2016).

[2] V. Baltz, A. Manchon, M. Tsoi, T. Moriyama, T. Ono, and Y. Tserkovnyak, Antiferromagnetic spintronics, Rev. Mod. Phys. **90**, 015005 (2018).

[3] S. Nakatsuji, N. Kiyohara, and T. Higo, Large anomalous Hall effect in a non-collinear antiferromagnet at room temperature, Nature (London) **527**, 212 (2015).

[4] T. Chen, T. Tomita, S. Minami, M. Fu, T. Koretsune, M. Kitatani, I. Muhammad, D. Nishio-Hamane, R. Ishii, F. Ishii, R. Arita, and S. Nakatsuji, Anomalous transport due to Weyl fermions in the chiral antiferromagnets Mn_3X, X = Sn, Ge, Nat. Commun. **12**, 572 (2021).

[5] T. Higo and S. Nakatsuji, Thin film properties of the non-collinear Weyl antiferromagnet Mn_3Sn, J. Magn. Magn. Mater. **564**, 170176 (2022).

[6] Y. Otani and T. Higo, Domain structure and domain wall dynamics in topological chiral antiferromagnets from the viewpoint of magnetic octupole, Appl. Phys. Lett. **118**, 040501 (2021).

[7] T. Higo, K. Kondou, T. Nomoto, M. Shiga, S. Sakamoto, X. Chen, D. Nishio-Hamane, R. Arita, Y. Otani, S. Miwa, and S. Nakatsuji, Perpendicular full switching of chiral antiferromagnetic order by current, Nature (London) **607**, 474 (2022).

[8] M.-T. Suzuki, T. Koretsune, M. Ochi, and R. Arita, Cluster multipole theory for anomalous Hall effect in antiferromagnets, Phys. Rev. B **95**, 094406 (2017).

[9] T. Higo, D. Qu, Y. Li, C. L. Chien, Y. Otani, and S. Nakatsuji, Anomalous Hall effect in thin films of the Weyl antiferromagnet Mn_3Sn, Appl. Phys. Lett. **113**, 202402 (2018).

[10] L. Šmejkal, A. H. MacDonald, J. Sinova, S. Nakatsuji, and T. Jungwirth, Anomalous Hall antiferromagnets, Nat. Rev. Mater. **7**, 482 (2022).

[11] M. Wu, T. Chen, T. Nomoto, Y. Tserkovnyak, H. Isshiki, Y. Nakatani, T. Higo, T. Tomita, K. Kondou, R. Arita, S. Nakatsuji, and Y. Otani, Current-driven fast magnetic octupole domain-wall motion in noncollinear antiferromagnets, Nat. Commun. **15**, 4305 (2024).

[12] B. H. Rimmler, B. Pal, and S. S. P. Parkin, Non-collinear antiferromagnetic spintronics, Nat. Rev. Mater. **10**, 109 (2025).

[13] K. Kuroda, T. Tomita, M.-T. Suzuki, C. Bareille, A. Nugroho, P. Goswami, M. Ochi, M. Ikhlas, M. Nakayama, S. Akebi, R. Noguchi, R. Ishii, N. Inami, K. Ono, H. Kumigashira, A. Varykhalov, T. Muro, T. Koretsune, R. Arita, S. Shin *et al.*, Evidence for magnetic Weyl fermions in a correlated metal, Nat. Mater. **16**, 1090 (2017).

[14] M. Ikhlas, T. Tomita, T. Koretsune, M.-T. Suzuki, D. Nishio-Hamane, R. Arita, Y. Otani, and S. Nakatsuji, Large anomalous Nernst effect at room temperature in a chiral antiferromagnet, Nat. Phys. **13**, 1085 (2017).

[15] X. Li, L. Xu, L. Ding, J. Wang, M. Shen, X. Lu, Z. Zhu, and K. Behnia, Anomalous Nernst and Righi-Leduc effects in Mn_3Sn: Berry curvature and entropy flow, Phys. Rev. Lett. **119**, 056601 (2017).

[16] X. Chen, T. Higo, K. Tanaka, T. Nomoto, H. Tsai, H. Idzuchi, M. Shiga, S. Sakamoto, R. Ando, H. Kosaki, T. Matsuo, D. Nishio-Hamane, R. Arita, S. Miwa, and S. Nakatsuji, Octupole-driven magnetoresistance in an antiferromagnetic tunnel junction, Nature (London) **613**, 490 (2023).

[17] S. S. P. Parkin, M. Hayashi, and L. Thomas, Magnetic domain-wall racetrack memory, Science **320**, 190 (2008).

[18] S. Emori, U. Bauer, S.-M. Ahn, E. Martinez, and G. S. D. Beach, Current-driven dynamics of chiral ferromagnetic domain walls, Nat. Mater. **12**, 611 (2013).

[19] M. S. Wörnle, P. Welter, M. Giraldo, T. Lottermoser, M. Fiebig, P. Gambardella, and C. L. Degen, Coexistence of Bloch and Néel walls in a collinear antiferromagnet, Phys. Rev. B **103**, 094426 (2021).

[20] X. Li, C. Collignon, L. Xu, H. Zuo, A. Cavanna, U. Gennser, D. Mailly, B. Fauqué, L. Balents, Z. Zhu, and K. Behnia, Chiral domain walls of Mn_3Sn and their memory, Nat. Commun. **10**, 3021 (2019).

[21] S. Sugimoto, Y. Nakatani, Y. Yamane, M. Ikhlas, K. Kondou, M. Kimata, T. Tomita, S. Nakatsuji, and Y. Otani, Electrical nucleation, displacement, and detection of antiferromagnetic domain walls in the chiral antiferromagnet Mn_3Sn, Commun. Phys. **3**, 111 (2020).

[22] T. Nagamiya, S. Tomiyoshi, and Y. Yamaguchi, Triangular spin configuration and weak ferromagnetism of Mn_3Sn and Mn_3Ge, Solid State Commun. **42**, 385 (1982).

[23] S. Tomiyoshi, Polarized neutron diffraction study of the spin structure of Mn_3Sn, J. Phys. Soc. Jpn. **51**, 803 (1982).

[24] S. Tomiyoshi and Y. Yamaguchi, Magnetic structure and weak ferromagnetism of Mn_3Sn studied by polarized neutron diffraction, J. Phys. Soc. Jpn. **51**, 2478 (1982).

[25] P. J. Brown, V. Nunez, F. Tasset, J. B. Forsyth, and P. Radhakrishna, Determination of the magnetic structure of Mn_3Sn using generalized neutron polarization analysis, J. Phys.: Condens. Matter **2**, 9409 (1990).

[26] M. Kimata, N. Sasabe, K. Kurita, Y. Yamasaki, C. Tabata, Y. Yokoyama, Y. Kotani, M. Ikhlas, T. Tomita, K. Amemiya, H. Nojiri, S. Nakatsuji, T. Koretsune, H. Nakao, T.-h. Arima, and T. Nakamura, X-ray study of ferroic octupole order producing anomalous Hall effect, Nat. Commun. **12**, 5582 (2021).

[27] H. Tsai, T. Higo, K. Kondou, T. Nomoto, A. Sakai, A. Kobayashi, T. Nakano, K. Yakushiji, R. Arita, S. Miwa, Y.

Otani, and S. Nakatsuji, Electrical manipulation of a topological antiferromagnetic state, Nature (London) **580**, 608 (2020).

[28] Y. Takeuchi, Y. Yamane, J.-Y. Yoon, R. Itoh, B. Jinnai, S. Kanai, J. Ieda, S. Fukami, and H. Ohno, Chiral-spin rotation of non-collinear antiferromagnet by spin–orbit torque, Nat. Mater. **20**, 1364 (2021).

[29] G. K. Krishnaswamy, G. Sala, B. Jacot, C.-H. Lambert, R. Schlitz, M. D. Rossell, P. Nöel, and P. Gambardella, Time-dependent multistate switching of topological antiferromagnetic order in Mn_3Sn, Phys. Rev. Appl. **18**, 024064 (2022).

[30] M. Ikhlas, S. Dasgupta, F. Theuss, T. Higo, S. Kittaka, B. J. Ramshaw, O. Tchernyshyov, C. W. Hicks, and S. Nakatsuji, Piezomagnetic switching of the anomalous Hall effect in an antiferromagnet at room temperature, Nat. Phys. **18**, 1086 (2022).

[31] T. Nomoto and R. Arita, Cluster multipole dynamics in noncollinear antiferromagnets, Phys. Rev. Res. **2**, 012045(R) (2020).

[32] M. Wu, K. Kondou, Y. Nakatani, T. Chen, H. Isshiki, T. Higo, S. Nakatsuji, and Y. Otani, Magnetic octupole domain evolution and domain-wall structure in the noncollinear Weyl antiferromagnet Mn_3Ge, APL Mater. **11**, 081115 (2023).

[33] X. Liu, Q. Feng, D. Zhang, Y. Deng, S. Dong, E. Zhang, W. Li, Q. Lu, K. Chang, and K. Wang, Topological spin textures in a non-collinear antiferromagnet system, Adv. Mater. **35**, 2211634 (2023).

[34] T. Higo, H. Man, D. B. Gopman, L. Wu, T. Koretsune, O. M. J. van 't Erve, Y. P. Kabanov, D. Rees, Y. Li, M.-T. Suzuki, S. Patankar, M. Ikhlas, C. L. Chien, R. Arita, R. D. Shull, J. Orenstein, and S. Nakatsuji, Large magneto-optical Kerr effect and imaging of magnetic octupole domains in an antiferromagnetic metal, Nat. Photon. **12**, 73 (2018).

[35] T. Uchimura, J.-Y. Yoon, Y. Sato, Y. Takeuchi, S. Kanai, R. Takechi, K. Kishi, Y. Yamane, S. DuttaGupta, J. Ieda, H. Ohno, and S. Fukami, Observation of domain structure in non-collinear antiferromagnetic Mn_3Sn thin films by magneto-optical Kerr effect, Appl. Phys. Lett. **120**, 172405 (2022).

[36] N. Hedrich, K. Wagner, O. V. Pylypovskyi, B. J. Shields, T. Kosub, D. D. Sheka, D. Makarov, and P. Maletinsky, Nanoscale mechanics of antiferromagnetic domain walls, Nat. Phys. **17**, 574 (2021).

[37] A. K. C. Tan, H. Jani, M. Högen, L. Stefan, C. Castelnovo, D. Braund, A. Geim, A. Mechnich, M. S. G. Feuer, H. S. Knowles, A. Ariando, P. G. Radaelli, and M. Atatüre, Revealing emergent magnetic charge in an antiferromagnet with diamond quantum magnetometry, Nat. Mater. **23**, 205 (2024).

[38] S. Li, M. Huang, H. Lu, N. J. McLaughlin, Y. Xiao, J. Zhou, E. E. Fullerton, H. Chen, H. Wang, and C. R. Du, Nanoscale magnetic domains in polycrystalline Mn_3Sn films imaged by a scanning single-spin magnetometer, Nano Lett. **23**, 5326 (2023).

[39] See Supplemental Material at http://link.aps.org/supplemental/10.1103/njnm-nl6n for detail of the quantum scanning magnetometry; raw data of Fig. 3(a); derivation of the reconstruction formula [Eq. (1)]; magnetization offset; magnetized axis determination; numerical verification of the method to estimate magnetized direction; observation of the tilted magnetization; domain flipping at coercive field; finite y-component of magnetization inside domain walls; domain wall fitting to other models; domain wall model with multiple easy axes; anisotropic domain shape; numerical prediction of stray field for [0001] domain walls reinforces the chiral domain wall; numerical prediction of stray field for $[2\bar{1}\bar{1}0]$ domain walls.

[40] N. Hedrich, D. Rohner, M. Batzer, P. Maletinsky, and B. J. Shields, Parabolic diamond scanning probes for single-spin magnetic field imaging, Phys. Rev. Appl. **14**, 064007 (2020).

[41] F. Casola, T. van der Sar, and A. Yacoby, Probing condensed matter physics with magnetometry based on nitrogen-vacancy centres in diamond, Nat. Rev. Mater. **3**, 17088 (2018).

[42] D. A. Broadway, S. E. Lillie, S. C. Scholten, D. Rohner, N. Dontschuk, P. Maletinsky, J.-P. Tetienne, and L. C. L. Hollenberg, Improved current density and magnetization reconstruction through vector magnetic field measurements, Phys. Rev. Appl. **14**, 024076 (2020).

[43] J. Liu and L. Balents, Anomalous Hall effect and topological defects in antiferromagnetic Weyl semimetals: Mn_3Sn/Ge, Phys. Rev. Lett. **119**, 087202 (2017).

[44] Q.-C. Sun, T. Song, E. Anderson, A. Brunner, J. Förster, T. Shalomayeva, T. Taniguchi, K. Watanabe, J. Gräfe, R. Stöhr, X. Xu, and J. Wrachtrup, Magnetic domains and domain wall pinning in atomically thin $CrBr_3$ revealed by nanoscale imaging, Nat. Commun. **12**, 1989 (2021).

[45] P. Appel, B. J. Shields, T. Kosub, N. Hedrich, R. Hübner, J. Faßbender, D. Makarov, and P. Maletinsky, Nanomagnetism of magnetoelectric granular thin-film antiferromagnets, Nano Lett. **19**, 1682 (2019).

[46] J.-P. Tetienne, T. Hingant, L. Martínez, S. Rohart, A. Thiaville, L. H. Diez, K. Garcia, J.-P. Adam, J.-V. Kim, J.-F. Roch, I. Miron, G. Gaudin, L. Vila, B. Ocker, D. Ravelosona, and V. Jacques, The nature of domain walls in ultrathin ferromagnets revealed by scanning nanomagnetometry, Nat. Commun. **6**, 6733 (2015).

[47] S. Vélez, J. Schaab, M. S. Wörnle, M. Müller, E. Gradauskaite, P. Welter, C. Gutgsell, C. Nistor, C. L. Degen, M. Trassin, M. Fiebig, and P. Gambardella, High-speed domain wall racetracks in a magnetic insulator, Nat. Commun. **10**, 4750 (2019).

[48] A. P. Malozemoff and J. C. Slonczewski, *Magnetic Domain Walls in Bubble Materials: Advances in Materials and Device Research* (Academic Press, New York, 1979).

[49] J.-Y. Yoon, P. Zhang, C.-T. Chou, Y. Takeuchi, T. Uchimura, J. T. Hou, J. Han, S. Kanai, H. Ohno, S. Fukami, and L. Liu, Handedness anomaly in a non-collinear antiferromagnet under spin–orbit torque, Nat. Mater. **22**, 1106 (2023).

[50] L. Néel, Énergie des parois de Bloch dans les couches minces, C. R. Acad. Sci. **241**, 533 (1955).

[51] Y. Araki, Magnetic textures and dynamics in magnetic weyl semimetals, Ann. Phys. (NY) **532**, 1900287 (2020).

[52] A. Ozawa, Y. Araki, and K. Nomura, Chiral gauge field in fully spin-polarized magnetic Weyl semimetal with magnetic domain walls, J. Phys. Soc. Jpn. **93**, 094704 (2024).